Supplementary Information

Unravelling the structure of chemisorbed CO_2 species in mesoporous aminosilicas: a critical survey

Rui Afonso, Mariana Sardo, Luís Mafra, José R. B. Gomes

CICECO – Aveiro Institute of Materials, Department of Chemistry, University of Aveiro, Campus Universitário de Santiago, 3810-193 Aveiro, Portugal

Table of Contents

1. Experimental details

1.1. Preparation of materials

SBA-15 was prepared as described in the literature [1]. Briefly, 4.0 g of co-polymer $(EO)_{20}(PO)_{70}(EO)_{20}$ (Aldrich) was dissolved in 126 cm^3 of 1.6 M HCl solution. Then, 9.1 cm^3 of tetraethyl orthosilicate (TEOS) – (Aldrich) was added with constant stirring. The solution was then stirred at 35 °C for 24 h and subsequently heated at 100 °C for 24 h, under static conditions. The obtained solid was filtered and dried in air. After, the solid was calcined at 550 °C for 5 h with a ramp of 1 °C/min. The resulting material (SBA-15) was stored in a desiccator for further use.

Dryness conditions of the reaction media and material are of paramount importance to prevent extension of lateral silane polymerization within the materials and to allow an efficient silane functionalization. To achieve this, typically 2 g of SBA-15 were introduced in a closed reflux apparatus connected to a vacuum line and heated overnight at 140 °C. After cooling, the nitrogen was introduced into the system prior to the opening of the reflux apparatus, and SBA-15 was refluxed with 100 cm^3 of dry toluene (Aldrich, 99.8 %) containing 9 mmol (high loading sample) of the 3-aminopropyltriethoxysilane (APTES, Aldrich, >98%) for 24 h in a nitrogen atmosphere. The resulting material was purified by Soxhlet extraction with dry toluene, to remove the unreacted amino-organosilanes, and finally dried under vacuum, at 120 °C for 24 h. The low amine loading sample was synthesized according to the literature [2]. Firstly, 0.35 g of SBA-15 was dried in the vacuum line by heating at 140 °C for 8 h. Next, SBA-15 was suspended in the mixture of 3.5 cm^3 of anhydrous toluene and 65 cm^3 of (3-triethoxysilylpropyl)-tert-butylcarbamate (TESPtBC, Gelest). The suspension was heated at 80 °C, under reflux, for 12 h. Lastly, the material was filtered out and washed with toluene. To remove the organic part that protects the amine, the sample was placed in a zirconia NMR rotor, degassed and heated for 6 h at 250 °C in our sorption apparatus (fully described below).

1.2. Sorption Apparatus

The sorption apparatus comprised a laboratory made high vacuum line, connected to a turbomolecular pumping station (HiCube 80, Pfeiffer Vacuum), capable of vacuum

greater than 10^{-2} Pa. A borosilicate glass cell, adapted from the description in the literature, was connected to the vacuum line and served as an enclosure for an NMR rotor allowing to degas and heat zirconia NMR rotors up to 300 °C under vacuum. The heating was performed with a laboratory made oven connected to a power controller (Eurotherm 3116), and the temperature measured with a thermocouple. The desired gas was introduced into the system from the canister connected to the vacuum line and the cell. The pressure inside the cell was measured with a capacitance transducer (MKS instruments, Baratron 722B).

1.3. Loading the Samples with $^{13}CO_2$

All samples were packed in zirconia NMR rotor, enclosed into the sorption apparatus and dried by degassing and heating. After cooling down under vacuum, $^{13}CO_2$ (Cortecnet, 99 atom % ^{13}C; < 3 atom % ^{18}O) was introduced into the system up to the desired partial pressure and allowed to equilibrate for 3 h. If needed, the cell was then filled with helium (Air Liquide, 99.999 %) up to the atmospheric pressure. Finally, the NMR rotor was closed inside the cell and only then the cell was open to remove the rotor for NMR measurements.

1.4. Computational details

The clusters used to model the silica surface are based on the experimental crystallographic structure of alpha-quartz [3] using the atomic positions of the silicon and oxygen atoms. Dangling bonds at the edges of the cluster models due to elimination of Si atoms were saturated with H atoms along the O−Si directions of the perfect crystal and imposing an O−H distance equal to 0.96 Å [4]. Note that although the real surface of mesoporous silicas is amorphous, using a surface built from a crystalline structure should not dramatically influence the results from the calculations, as we are dealing with relatively small clusters.

The silylpropylamines were grafted (through optimisation) on the clusters where OH groups existed, each binding three surface OH groups. Subsequent optimisations of different species involved the relaxation of the alkyl chain (and the respective functional group at its end), water or CO_2 molecules (when present), the SiO_3 moieties binding the alkylamines, and the surface OH groups, while the remaining Si and O atoms were kept frozen at their crystallographic positions. The fixation of some atomic

positions provides a simple but effective representation of the mechanical embedding of the solid covalent oxide surface [5-6]. The absence of imaginary values in the frequencies involving the atoms optimised in the different structural models ensured that the structures are true minima on their potential energy surfaces. However, to model some specific structures, it was necessary to fix specific structural parameters at no optimal values which led to vibrational modes with associated imaginary wavenumbers.

Three different sized clusters (Figure S1) were used in this work; a small cluster, with a single amine chain and a single surface silanol, a medium cluster, with two amine chains and a surface silanol, and a large cluster, with one amine chain and five surface silanols. The cluster models are based on six (small), nine (medium) and fourteen (large) Si atoms and, following the notation used by López et al. [5] will be named as N-T models (N=6, 9 or 14, respectively). The tests in our previous study [7] indicate that their sizes are adequate to prevent spurious border effects.

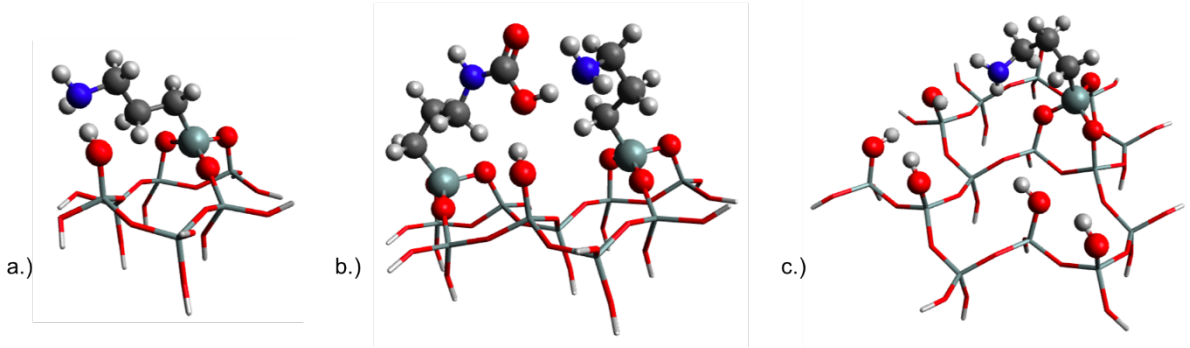

Figure S1. Three-dimensional representations of the three clusters used in this work; (a) small cluster, 6-T, (b) medium cluster, 9-T, (c) large cluster, 14-T. Stick and ball-and-stick representations denote frozen and fully optimised atoms, respectively. Colour code is: white, H; dark grey, C; blue, N; red, O; and light grey, Si.

To model a very specific case of an isolated amine, not able to form hydrogen bonds with the silica framework, we have also employed a $(CH_3)_3SiCH_2CH_2CH_2NH_2$ model, where terminating OH moieties were replaced by non-interacting methyl groups.

The M06-2X hybrid functional based on the meta-generalized gradient approximation of Truhlar and Zhao [8-9] and the standard 6-31G(d) basis set [10-11], with a single

polarisation function in all the atoms except hydrogen, as included in the Gaussian 09 software [12], were used in all the structural optimisations, in the calculation of electronic energies or Gibbs energies at *T*=298.15 K, and vibrational frequencies. The combination of the M06 family of functionals and Gaussian-type orbitals basis sets with cluster models was found to provide geometries, energies, and frequencies in very good agreement with available experimental data for several systems [13-16] that are challenging for DFT approaches from the lower rungs of the Jacob's ladder of density functional approximations [17]. The M06-2X functional has been suggested for geometry optimization in a guide to small-molecule structure assignment through computation of some NMR chemical shifts [18], so it has been the default choice in our work with amine-functionalised silicas [7, 19]. In all calculations, the default integration grids and convergence thresholds in the Gaussian 09 software were employed [12]. As common practice, the calculated wavenumbers were multiplied by a scale factor; the value used (0.947) was optimised for the M06-2X/6-31G(d) approach and was taken from ref. [20].

NMR shielding tensors of the optimized geometries have been computed with the GIAO method [21-22], also using the M06-2X functional and the 6-31G(d) basis set. These conditions typically create relatively small root-mean-square errors of the calculated ^{13}C chemical shifts (cf. 3.2 ppm) [23]. No such reference result exists for ^{15}N, computed at the M06-2X/6-31G(d) level of theory, so we calculated it ourselves for a set of experimental chemical shifts of aqueous alkylamines [24], having obtained a root-mean-square error of 4.9 ppm using an implicit solvent method, the polarisable continuum model (PCM) [25] (Table S25). The isotropic magnetic shielding tensors calculated for the clusters were subtracted from those calculated for a reference, to obtain the chemical shift relative to such reference. The reference for ^{13}C chemical shifts was gas-phase tetramethylsilane (at 0 ppm, as in our previous work [7, 26]), and for ^{15}N chemical shifts it was the α-glycine crystalline structure (at 33.4 ppm). Within the cluster model approach, the latter compound was modelled as a cluster composed by a central glycine molecule and its 26 nearest neighbours (Figure S8) with atomic positions taken from the periodic structure of α-glycine [27]. The five hydrogen atoms of the central molecule were fully optimized while the remaining atomic positions were left unchanged for an adequate embedding.

1.5. NMR measurements

^{13}C NMR spectra were acquired at room temperature on a Bruker Avance III 700 spectrometer operating at B_0 field of 16.4 T with ^{13}C frequency of 176.1 MHz. All experiments were performed on a double-resonance 4 mm probe and samples were packed into ZrO_2 rotors with Kel-F (4 mm) caps. Spinning rate of 12 kHz was employed to record all spectra. ^{13}C chemical shifts are quoted in ppm from TMS (0 ppm) and α-glycine (secondary reference, C=O at 176.03 ppm). ^{13}C CPMAS spectra were acquired under the following experimental conditions: ^{1}H 90° pulse was set to 3.0 μs corresponding to a radio-frequency of 83 kHz; the CP step was performed with a contact time of 2000 μs using a 50−100% RAMP shape on the ^{1}H channel and a radio-frequency of 77 kHz and a 50 kHz square shape pulse was used on the ^{13}C channel. Recycle delay was 4 s for all measurements. During the acquisition, a SPINAL-64 decoupling scheme was employed using a pulse length for the basic decoupling units of 5.6 μs at rf field strength of 83 kHz.

2. Chemical shifts and lowest energy models for amine/ammonium species

Table S1. Calculated ^{15}N chemical shifts for different amine and ammonium species (based on Tables S2-S4) together with the experimental values from Chen et al. [28]. Corresponding structures shown in Figure S2, using the same labels.

Label	Species	Calculated	Experimental	Tables
10	Amine	δ_N = 27.9 ppm	δ_N = 24 ppm	Table S2 17 Structures
11	Ammonium Siloxide	δ_N = 33.1 ppm	δ_N = 32 ppm	Table S3 16 Structures
12	Dithered Amine	δ_N = 45.1 ppm	δ_N = 44 ppm	Table S4 14 Structures

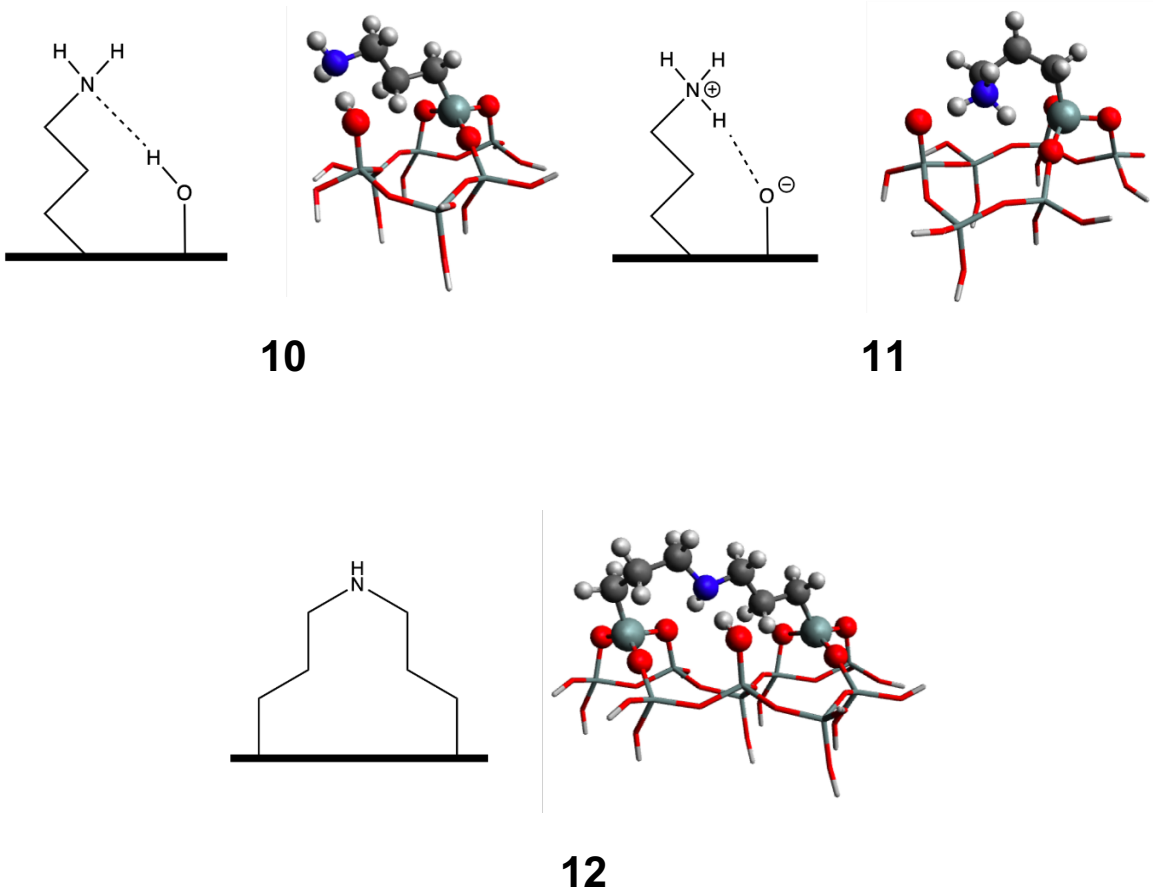

Figure S2. 2D and 3D structural representations of different amine/ammonium species. 3D representations are lowest-energy optimised structures. Stick and ball-and-stick representations denote frozen and fully optimised atoms, respectively. Colour code is: white, H; dark grey, C; blue, N; red, O; and light grey, Si. Structures are associated with the values presented in Table S1 (same labels used).

3. Optimised structural models

3.1. Amine

Table S2. Results of optimisation trials of the amine-silanol cluster. Energy differences to the most stable structure (**10**) and corresponding ^{15}N chemical shifts are shown for the different structures.

Structure	ΔE (kJ·mol^{-1})	δ_N (ppm)
Structure i	18	27.0
Structure ii	18	27.6
Structure iii	16	24.3
Structure iv	15	31.5
Structure v	13	22.2
Structure vi	12	31.6
Structure vii	11	22.6
Structure viii	11	27.2
Structure ix	10	27.2
Structure x	9	22.6
Structure xi	9	21.9
Structure xii	8	23.6
Structure xiii	7	30.6
Structure xiv	7	26.1
Structure xv	6	31.5
Structure xvi	3	25.7
Structure xvii	0	27.9

3.2. Ammonium Siloxide

Table S3. Results of optimisation trials of the ammonium siloxide cluster. Energy differences to the most stable structure (**11**) and corresponding ^{15}N chemical shifts are shown for the different structures.

Structure	ΔE (kJ·mol^{-1})	δ_N (ppm)
Structure i	25	33.2
Structure ii	25	37.8
Structure iii	23	39.8
Structure iv	19	36.3
Structure v	18	36.2
Structure vi	15	28.8
Structure vii	14	31.6
Structure viii	13	37.9
Structure ix	12	29.1
Structure x	12	31.3
Structure xi	11	34.2
Structure xii	10	37.8
Structure xiii	9	29.9
Structure xiv	6	34.0
Structure xv	5	29.3
Structure xvi	0	33.1

3.3. Ditethered amine

Table S4. Results of optimisation trials of the di-tethered amine-silanol cluster. Energy differences to the most stable structure (**12**) and corresponding ^{15}N chemical shifts are shown for the different structures.

Structure	ΔE (kJ·mol^{-1})	δ_N (ppm)
Structure i	115	52.1
Structure ii	85	35.6
Structure iii	67	36.7
Structure iv	61	52.0
Structure v	49	40.4
Structure vi	37	40.9
Structure vii	35	40.2
Structure viii	31	54.9
Structure ix	23	51.9
Structure x	22	41.0
Structure xi	20	45.7
Structure xii	14	46.5
Structure xiii	12	42.7
Structure xiv	0	45.1

Table S5. Results of optimisation trials of the di-tethered amine-silanol cluster, with an added carbon dioxide molecule. Energy differences to the most stable structure and corresponding ^{15}N chemical shifts are shown for the different structures.

Structure	ΔE (kJ·mol^{-1})	δ_N (ppm)
Structure i	12	46.2
Structure ii	11	46.1
Structure iii	10	45.9
Structure iv	8	45.7
Structure v	0	46.3

3.4. Ammonium carbamate

Table S6. Results of optimisation trials of the ammonium carbamate cluster. Energy differences to the most stable structure (**1**) and corresponding ^{15}N and ^{13}C chemical shifts are shown for the different structures. The two ^{15}N chemical shifts correspond to nitrogen atoms in the ammonium and carbamate functional groups.

Structure	ΔE (kJ·mol^{-1})	δ_{N1} (ppm)	δ_{N2} (ppm)	δ_{C} (ppm)
Structure i	181	26.2	90.8	161.1
Structure ii	159	29.2	95.7	163.7
Structure iii	100	33.1	84.1	168.1
Structure iv	96	31.3	93.7	167.0
Structure v	89	35.7	86.4	172.0
Structure vi	85	33.7	91.7	166.9
Structure vii	84	38.9	92.8	169.1
Structure viii	84	33.7	91.2	168.5
Structure ix	84	37.1	87.4	168.6
Structure x	83	29.5	89.1	170.2
Structure xi	83	34.5	88.7	169.6
Structure xii	80	33.8	87.3	163.8
Structure xiii	80	29.2	92.4	162.4
Structure xiv	79	26.7	90.6	169.9
Structure xv	75	34.9	89.6	168.4
Structure xvi	71	32.2	90.6	169.8
Structure xvii	70	29.0	89.9	170.0
Structure xviii	69	35.6	91.8	168.2
Structure xix	62	34.2	93.5	167.6
Structure xx	7	29.2	90.2	164.7
Structure xxi	0	34.5	90.4	163.7

3.5. Carbamic acid (2 amines, 1 silanol)

Table S7. Results of optimisation trials of the carbamic acid cluster containing 2 amines and 1 silanol. Energy differences to the most stable structure (**2**) and corresponding ^{15}N and ^{13}C chemical shifts are shown for the different structures. The two ^{15}N chemical shifts correspond to nitrogen atoms in the amine and carbamic acid functional groups.

Structure	ΔE (kJ·mol^{-1})	δ_{N1} (ppm)	δ_{N2} (ppm)	δ_C (ppm)
Structure i	82	27.3	84.2	155.1
Structure ii	78	27.9	84.4	156.1
Structure iii	75	31.6	83.9	155.4
Structure iv	68	34.8	92.2	165.2
Structure v	59	33.7	88.2	163.9
Structure vi	58	33.5	89.9	156.9
Structure vii	54	35.4	89.8	158.3
Structure viii	53	36.5	90.2	161.0
Structure ix	50	34.0	90.9	162.9
Structure x	49	26.4	97.6	161.8
Structure xi	49	29.0	90.9	165.7
Structure xii	49	35.2	87.0	158.1
Structure xiii	46	26.8	92.7	164.9
Structure xiv	45	32.5	87.0	163.8
Structure xv	42	41.3	94.9	158.9
Structure xvi	42	42.6	94.2	159.0
Structure xvii	41	44.0	93.2	161.9
Structure xviii	38	35.5	88.3	161.8
Structure xix	35	28.3	91.4	165.6
Structure xx	34	30.5	87.6	163.8
Structure xxi	34	35.0	92.2	162.9
Structure xxii	32	29.6	93.7	163.7
Structure xxiii	5	36.1	93.4	164.7
Structure xxiv	5	36.1	88.3	159.9
Structure xxv	0	31.7	91.2	159.3

3.6. Carbamic acid (2 amines, 0 silanols)

Table S8. Results of optimisation trials of the carbamic acid cluster containing 2 amines and 0 silanols. Energy differences to the most stable structure (**3**) and corresponding ^{15}N and ^{13}C chemical shifts are shown for the different structures. The two ^{15}N chemical shifts correspond to nitrogen atoms in the amine and carbamic acid functional groups.

Structure	ΔE (kJ·mol^{-1})	δ_{N1} (ppm)	δ_{N2} (ppm)	δ_C (ppm)
Structure i	86	26.4	88.1	157.1
Structure ii	64	27.8	87.4	158.1
Structure iii	62	24.9	89.4	160.8
Structure iv	45	16.7	87.9	161.4
Structure v	43	31.2	84.9	161.8
Structure vi	35	31.4	81.9	160.3
Structure vii	34	31.1	85.5	159.7
Structure viii	27	22.8	78.9	161.1
Structure ix	25	27.3	87.7	160.3
Structure x	6	30.3	94.8	163.4
Structure xi	4	38.5	89.4	160.9
Structure xii	0	31.7	92.6	161.8

3.7. Carbamic acid (1 amine, 1 silanol)

Table S9. Results of optimisation trials of the carbamic acid cluster containing 1 amine and 1 silanol. Energy differences to the most stable structure (**4**) and corresponding ^{15}N and ^{13}C chemical shifts are shown for the different structures.

Structure	ΔE (kJ·mol^{-1})	δ_N (ppm)	δ_C (ppm)
Structure i	24	83.6	152.4
Structure ii	11	93.4	162.4
Structure iii	6	77.6	152.0
Structure iv	5	81.4	161.5
Structure v	0	83.3	158.2

3.8. Carbamic acid (1 amine, 5 silanols)

Table S10. Results of optimisation trials of the carbamic acid cluster containing 1 amine and 5 silanols. Energy differences to the most stable structure (**5**) and corresponding ^{15}N and ^{13}C chemical shifts are shown for the different structures.

Structure	ΔE (kJ·mol^{-1})	δ_N (ppm)	δ_C (ppm)
Structure i	82	88.7	151.1
Structure ii	59	94.9	162.0
Structure iii	59	83.3	157.2
Structure iv	52	88.0	157.8
Structure v	48	99.5	164.4
Structure vi	47	98.3	160.9
Structure vii	41	86.5	158.9
Structure viii	39	99.6	159.6
Structure ix	34	97.3	160.4
Structure x	34	90.6	161.4
Structure xi	31	97.2	162.2
Structure xii	30	93.0	162.8
Structure xiii	30	87.6	163.7
Structure xiv	23	90.8	159.6
Structure xv	23	90.7	159.6
Structure xvi	0	96.2	156.1

3.9. Carbamic acid (1 amine, 0 silanols)

Table S11. Results of optimisation trials of the carbamic acid cluster containing 1 amine and 0 silanols. Energy differences to the most stable structure (**6**) and corresponding ^{15}N and ^{13}C chemical shifts are shown for the different structures.

Structure	ΔE (kJ·mol^{-1})	δ_N (ppm)	δ_C (ppm)
Structure i	8.1	83.3	153.2
Structure ii	5.4	85.3	155.5
Structure iii	5.3	83.8	153.2
Structure iv	4.2	83.6	153.2
Structure v	3.9	80.8	153.9
Structure vi	3.7	81.2	153.5
Structure vii	3.4	76.8	153.2
Structure viii	3.4	77.7	153.2
Structure ix	0.0	82.5	153.8

3.10. Ammonium bicarbonate

Table S12. Results of optimisation trials of the ammonium bicarbonate cluster. Energy differences to the most stable structure (**7**) and corresponding ^{15}N and ^{13}C chemical shifts are shown for the different structures.

Structure	ΔE (kJ·mol^{-1})	δ_N (ppm)	δ_C (ppm)
Structure i	42	34.0	160.3
Structure ii	34	34.2	165.7
Structure iii	33	32.3	161.5
Structure iv	30	34.1	162.4
Structure v	20	39.0	161.2
Structure vi	14	32.7	159.8
Structure vii	11	33.8	160.3
Structure viii	4	33.6	160.6
Structure ix	2	32.9	160.0
Structure x	1	36.9	160.4
Structure xi	0	37.5	162.0

3.11. Silylpropylcarbamate

Table S13. Results of optimisation trials of the silylpropylcarbamate cluster. Energy differences to the most stable structure (**8**) and corresponding ^{15}N and ^{13}C chemical shifts are shown for the different structures.

Structure	$\triangle E$ (kJ·mol^{-1})	δ_N (ppm)	δ_C (ppm)
Structure i	26	95.8	147.8
Structure ii	15	97.2	150.9
Structure iii	15	98.5	150.3
Structure iv	0	91.9	147.4

3.12. Ditethered carbamic acid

Table S14. Results of optimisation trials of the di-tethered carbamic acid cluster. Energy differences to the most stable structure (**9**) and corresponding ^{15}N and ^{13}C chemical shifts are shown for the different structures.

Structure	ΔE (kJ·mol^{-1})	δ_N (ppm)	δ_C (ppm)
Structure i	117	102.0	163.1
Structure ii	93	75.0	172.8
Structure iii	90	93.2	169.2
Structure iv	50	104.7	163.3
Structure v	30	93.7	163.4
Structure vi	5	101.9	161.6
Structure vii	4	91.1	154.6
Structure viii	1	100.2	158.6
Structure ix	0	100.2	158.5

4. Energetics

4.1. Single-tethered amine and ammonium

Compared structures correspond to Structure xvii of Table S2 for the amine (**10**, Figure S2), and Structure xvi of Table S3 for the ammonium (**11**, Figure S2).

Table S15. Comparison of Gibbs energy of formation of single-tethered amine (**10**) and ammonium (**11**).

Species	ΔG (kJ·mol^{-1})
Ammonium	99.6
Amine	0

4.2. Carbamic acid and ammonium carbamate

Compared structures correspond to Structure xxi of Table S6 for ammonium carbamate (**1,** Figure 1), and Structure xxv of Table S7 for carbamic acid (**2,** Figure 1).

Table S16. Comparison of Gibbs energy of formation of ammonium carbamate (**1**) and carbamic acid (**2**).

Species	ΔG (kJ·mol^{-1})
Ammonium carbamate	3.6
Carbamic acid	0

4.3. Single-tethered amine – silylpropylcarbamate, adsorbed CO_2 and carbamic acid

Energetic comparisons between different clusters can only be done if the same number and kinds of atoms are present. This is the case between clusters representing carbamic acid and adsorbed CO_2. However, silylpropylcarbamate has one less oxygen atom and two less hydrogen atoms. Therefore, a single water molecule was added to the model (and then optimised) to allow energetic comparisons with adsorbed CO_2 and carbamic acid.

We have chosen to not present the optimisation trials tables for the structures of silylpropylcarbamate and amine with adsorbed CO_2 but three-dimensional representations of the most stable structures are shown in Figure S3.

Table S17. Comparison of Gibbs energy of formation of silylpropylcarbamate (**13**, Figure S3), amine with adsorbed CO_2 (**14**, Figure S3) and carbamic acid (**4**, Figure 1). It was necessary to add a water molecule to the silylpropylcarbamate cluster, so a comparison could be made with the other two structures (i.e., for balancing the number of atoms).

Species	ΔG **(kJ·mol^{-1})**
Silylpropylcarbamate	30
Adsorbed CO_2	15
Carbamic acid	0

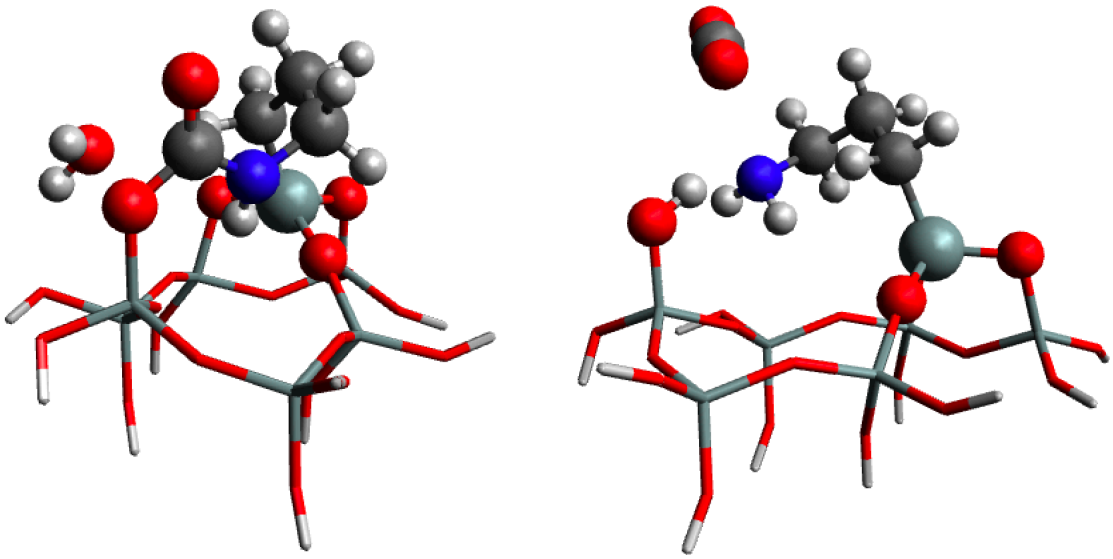

13

14

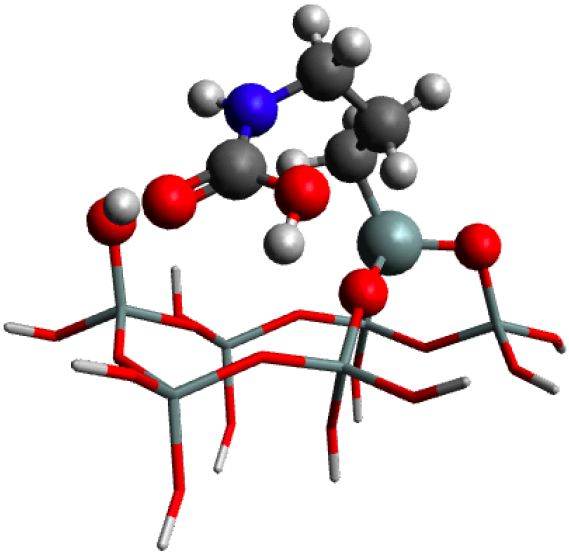

4

Figure S3. Three-dimensional structures of silylpropylcarbamate with a water molecule (**13**), of a primary amine with an adsorbed CO_2 molecule (**14**), and of carbamic acid interacting with a surface silanol (**4**), used in the energetic analysis of Table S17. The structures shown are lowest energy optimised structures from several different starting atomic arrangements. Atoms shown in stick representation were frozen during the optimisation procedure, while those in ball-and-stick representation were free to move.

4.4. Single-tethered amine – adsorbed CO_2, bicarbonate and carbamic acid

Just as in the previous section, energetic comparisons with bicarbonate demand the introduction of, at least, one water molecule. In this case, one water molecule was added to the adsorbed CO_2 and carbamic acid clusters. Notice that the ΔG between carbamic acid and adsorbed CO_2 is different in the presence or in the absence of the additional water molecule, showing how the introduction of a water molecule influences the energy of the cluster in different ways for different species.

As in the previous section, we have chosen to not present the full optimisation tables for each species. However, three-dimensional representations of the most stable structures are shown in Figure S4.

Table S18. Comparison of Gibbs energy of formation of adsorbed CO_2 (**15**, Figure S4), bicarbonate (**16**, Figure S4), and carbamic acid (**17**, Figure S4). It was necessary to add a water molecule to the carbamic acid and adsorbed CO_2 clusters, so a comparison could be made with bicarbonate (i.e., for balancing the number of atoms).

Species	ΔG **(kJ·mol^{-1})**
Adsorbed CO_2	26
Bicarbonate	12
Carbamic acid	0

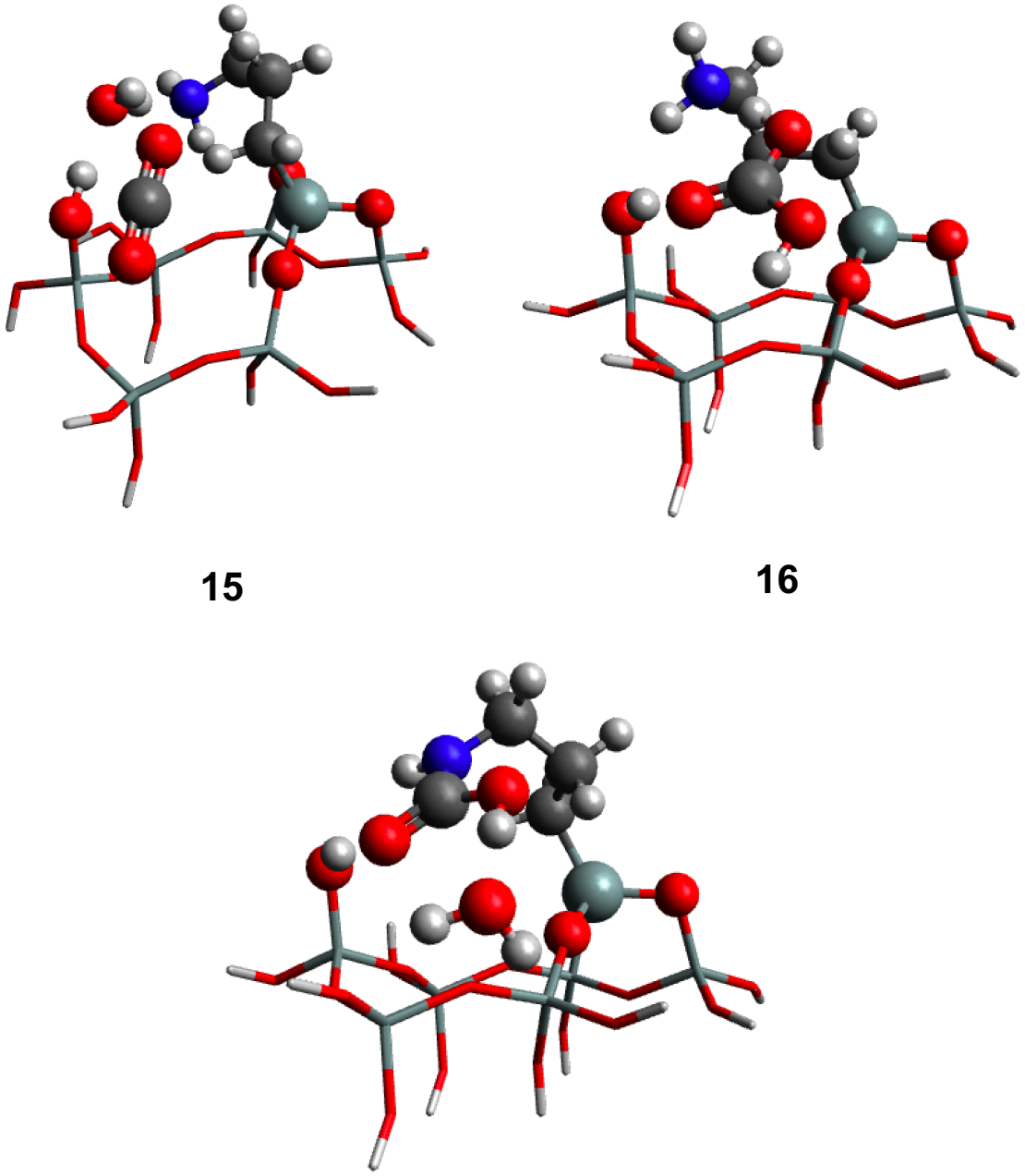

Figure S4. Three-dimensional structures of adsorbed CO_2, interacting with a surface silanol and a water molecule (**15**), of bicarbonate interacting with a surface silanol and a free amine (**16**), and of carbamic acid interacting with a surface silanol and a water molecule (**17**), used in the energetic analysis of Table S18. The structures shown are lowest energy optimised structures from several different starting atomic arrangements. Atoms shown in stick representation were frozen during the optimisation procedure, while those in ball-and-stick representation were free to move.

4.5. Ditethered amine

Table S19. Comparison of Gibbs energy of formation of ditethered carbamic acid and ditethered amine with adsorbed CO_2, respectively, **9** (Figure 1) and **12** (Figure S2)

Species	ΔG **(kJ·mol^{-1})**
Carbamic acid	70
Adsorbed CO_2	0

5. NMR Literature Review

Table S20. ^{13}C chemical shifts assignment taken from literature [2, 7, 26, 28-36]. Graphical representation at the bottom compares the experimental results with the calculated values (black lines with numeric labelling as in Figure 1) from this work.

Reference	Chemical shift / ppm	
	Carbamic Acid	Ammonium Carbamate
Pinto, 2011 [29]	160	164
Young, 2011 [2]	—	160
Mello, 2011 [30]	—	165.6
Sayari, 2012 [31]	160.5	164.6
Huang, 2014 [32]	—	164.2
Santos, 2015 [33]	—	162
Moore, 2015 [34]	160.3	162.8-168.8
Mafra, 2017 [7]	153.3[a]; 160.0	163.5
Chen, 2017 [28]	161	165
Milner, 2017 [35]	161.1	—
Foo, 2017 [36]	160.8	164.6
Čendak, 2018 [26]	153.6[a]; 160.6	164.0
Figure 2, top	153.7[a]; 161.3	164.3
Figure 2, bottom	152.6[a]; 159.5	164.1

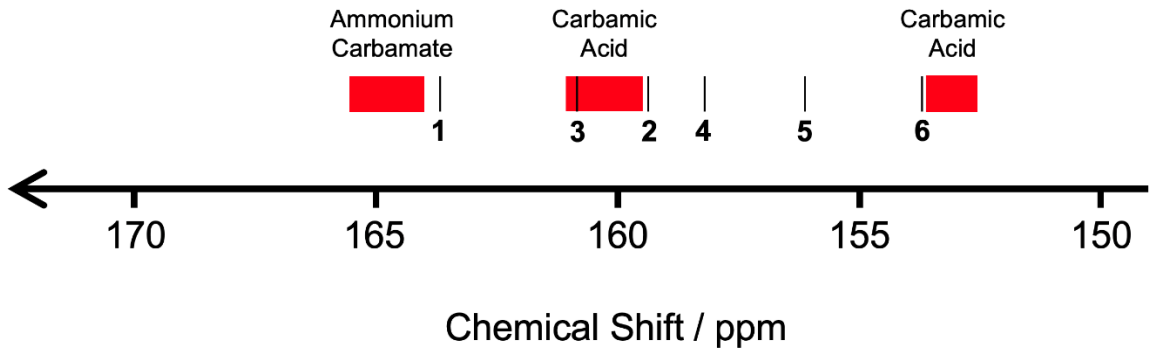

[a]Appears only under absolutely anhydrous conditions.

6. Infrared spectroscopy

6.1. Ammonium Carbamate and Carbamic Acid

Table S21. Comparison of experimental and calculated frequencies of the infrared spectrum of the samples of Shimon et al. [37]. Experimental values were taken from Table S4 of [37]. Alternative assignments are given when the calculated and experimental values are significantly different.

		Frequency / cm^{-1}		**Alternative**	
Species	**Assignment**	**Experimental**	**Calculated**	**Assignment**	**Calc. Freq. / cm^{-1}**
Carbamic acid (**2**)	ν C=O	1690	1755	—	—
Carbamic acid (**2**)	δ NCOO-H	—	1648	—	—
Ammonium (**1**)	δ_{asym} NH_3^+	1625	1644	—	—
Carbamate (**1**)	υ_{asym} COO^-	1580	1649	—	—
Carbamate (**1**)	υ_{asym} COO^-	1552	—	σ NH_2	1558
Ammonium (**1**)	δ_{asym} NH_3^+	1530	1515	—	—
Carbamic acid (**2**)	υ CN + δ NH	—	1519	—	—
Carbamate (**1**)	δ NH	1484	1481	—	—
Ammonium (**1**)	δ_{sym} NH_3^+	1473	—	—	—
Carbamate (**1**)	υ_{sym} COO^-	1437	1533	—	—
Carbamate (**1**)	υ_{sym} COO^-	1383	—	υ COO-H…NH_2	1403
Carbamic acid (**2**)	υ CN	1324	1519	υ SiO-H	1318
Carbamate (**1**)	υ CN	1324	1267	—	—
Carbamic acid (**2**)	τ COO-H…NH_2	—	1317	—	—
Carbamic acid (**2**)	OC-OH	—	1231	—	—

Table S22. Experimental and calculated vibrational frequencies for different functional groups in carbamic acid (**2** - **6**) and carbamate ion (**1**). Experimental frequencies taken from refs. [36, 38-48].

		Frequencies / cm^{-1}	
Species	**Assignment**	**Experimental**	**Calculated**
Carbamic acid	υ C=O	1680-1700	1798 (**6**)
			1732 (**4**)
			1733 (**5**)
			1705 (**3**)
			1755 (**2**)
Carbamate ion	υ_{asym} COO^-	1545-1567	1649 (**1**)
	υ_{sym} COO^-	1431-1442	1533 (**1**)
	δ NH	1480-1495	1481 (**1**)
	υ CN	1304-1332	1267 (**1**)

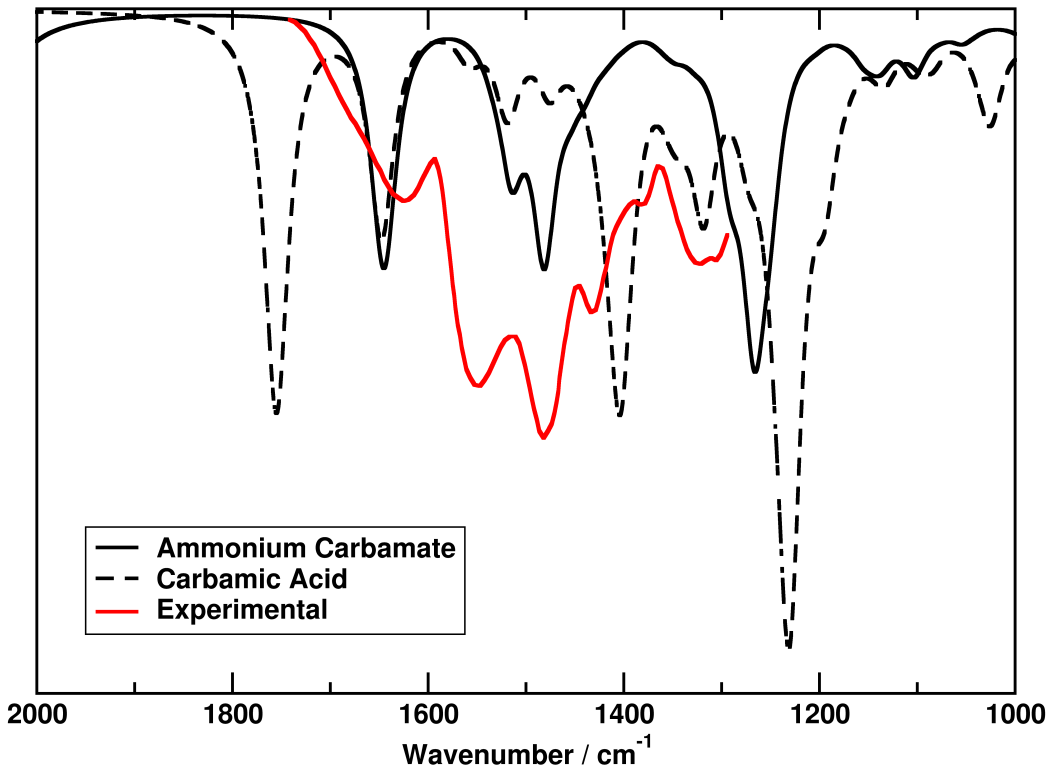

Figure S5. Calculated infrared spectra (in black) of ammonium carbamate (**1**) and carbamic acid (**2**) obtained using a Lorentzian function with 15 cm^{-1} full width at half maximum. The experimental infrared spectrum (in red) obtained by Shimon et al. [37] after 60 min of contact with CO_2 was taken with Engauge Digitizer [49] from printed graphs in the Supporting Information of the original reference.

The experimental spectrum obtained by Shimon et al. [37] is plotted in Figure S5 together with the calculated spectra for ammonium carbamate and carbamic acid models (further calculated data in Tables S21 and S22), which are the most abundant species according to ^{13}C NMR data. Other species, if present, are expected to have less important contributions to the experimental infrared spectrum. For both the carbamic acid (**2**) and the ammonium carbamate (**1**) cases, the structural models consider 2 amine molecules and 1 silanol group attached onto the silica surface. A significant overlap between experimental spectrum and the calculated spectra of the pure species can be observed. For instance, the experimental band at 1324 cm^{-1} seems to be well correlated with the 1317 cm^{-1} band in the calculated carbamic acid spectrum, which originates from COO–H twisting; the 1431 cm^{-1} experimental band may be correlated with the calculated 1403 cm^{-1} carbamic acid peak attributed to

COO–H(···NH_2) stretching; the 1482 and 1548 cm^{-1} experimental bands also seem to correlate well with the 1481 and 1515 cm^{-1} bands in the computed ammonium carbamate spectrum, originating from N–H bending and NH_3^+ symmetrical deformation modes, respectively. Finally, the experimental band at 1624 cm^{-1} probably stems from the 1644 and 1648 cm^{-1} wavenumbers of ammonium carbamate and carbamic acid, arising from NH_3^+ asymmetrical deformation and COO–H bending, respectively.

6.2. Silylpropylcarbamate

Table S23. Experimental and calculated vibrational frequencies for different functional groups in silylpropylcarbamate (**8**). Experimental frequencies were taken from refs. [41-44].

	Frequency / cm^{-1}	
Assignment	**Experimental**	**Calculated**
υ C=O	1715-1695	1799
υ N-H	3455	3410
δ N-H	1521-1510	1479

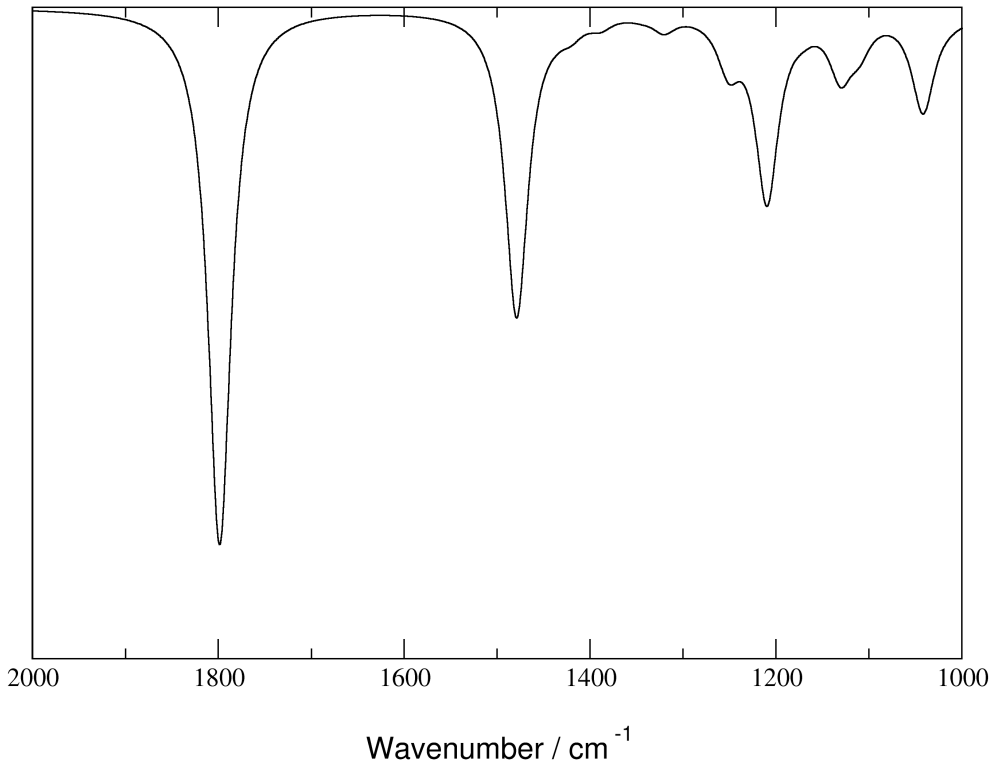

Figure S6. Calculated infrared spectrum of silylpropylcarbamate (**8**). Spectrum obtained with a Lorentzian function with 15 cm^{-1} full width at half maximum.

6.3. Ammonium bicarbonate

Table S24. Experimental and calculated vibrational frequencies for different functional groups in ammonium bicarbonate (**7**). Experimental frequencies taken from refs. [36, 44, 47-48, 50-52]. Alternative assignments are given when the calculated and experimental values are significantly different.

	Frequency / cm^{-1}		**Alternative**	
Assignment	**Experimental**	**Calculated**	**Assignment**	**Calc. Freq. / cm^{-1}**
υ_{asym} COO^-	1670-1616	1696	—	—
υ_{sym} COO^-	1360-1350	1385	—	—
C-O bend	1384-1382	—	ν_{sym} COO^-	1385
δ COH	1229	—	δ SiO-H	1188

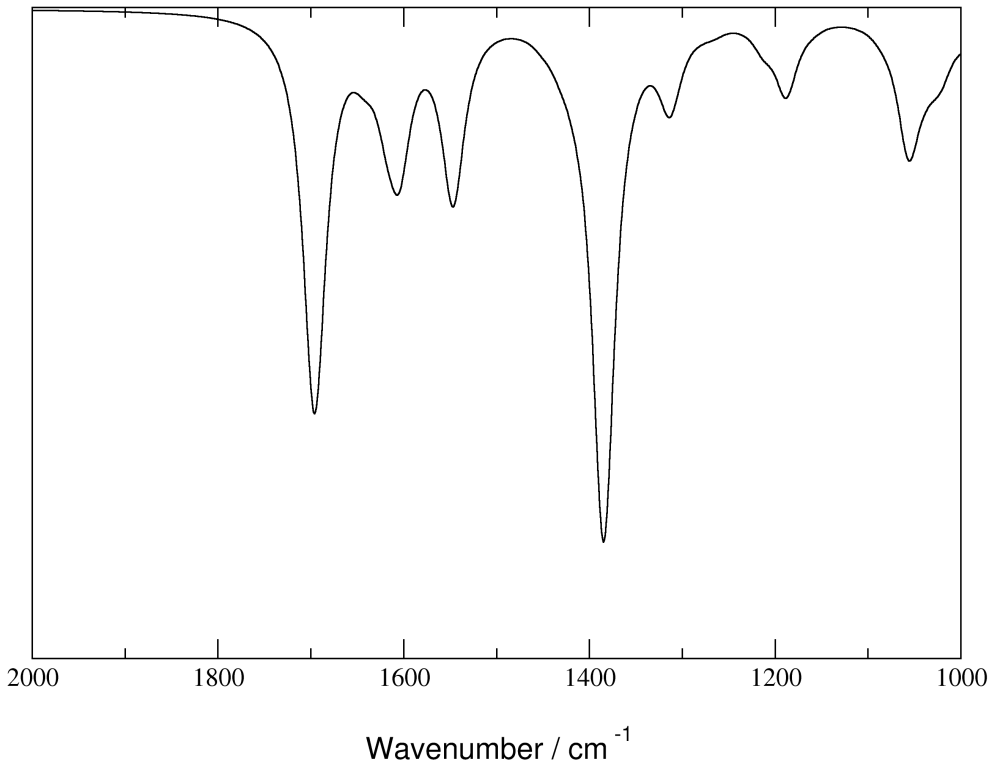

Figure S7. Calculated infrared spectrum of ammonium bicarbonate (**7**). Spectrum obtained with a Lorentzian function with 15 cm^{-1} full width at half maximum.

7. Root-mean-square error of ^{15}N chemical shift calculation

Table S25. Calculated and experimental data used to calculate the root-mean-square error (RMSE) of ^{15}N chemical shift calculation. Calculated values obtained with GIAO and the M06-2X/6-31G(d) approach and the polarisable continuum model (PCM) [25] for the implicit solvent. Experimental values taken from [24].

	Calculated	Experimental	Difference	Difference squared
Propylamine	32.05	25.23	6.82	46.5
Butylamine	30.28	25.40	4.88	23.9
Isobutylamine	24.30	22.15	2.15	4.6
Sec-butylamine	50.34	42.44	7.90	62.3
Isopropylamine	49.16	46.81	2.35	5.5
Tert-butylamine	61.90	60.87	1.03	1.1
			Average:	23.98
			Square root:	4.90

8. Other figures

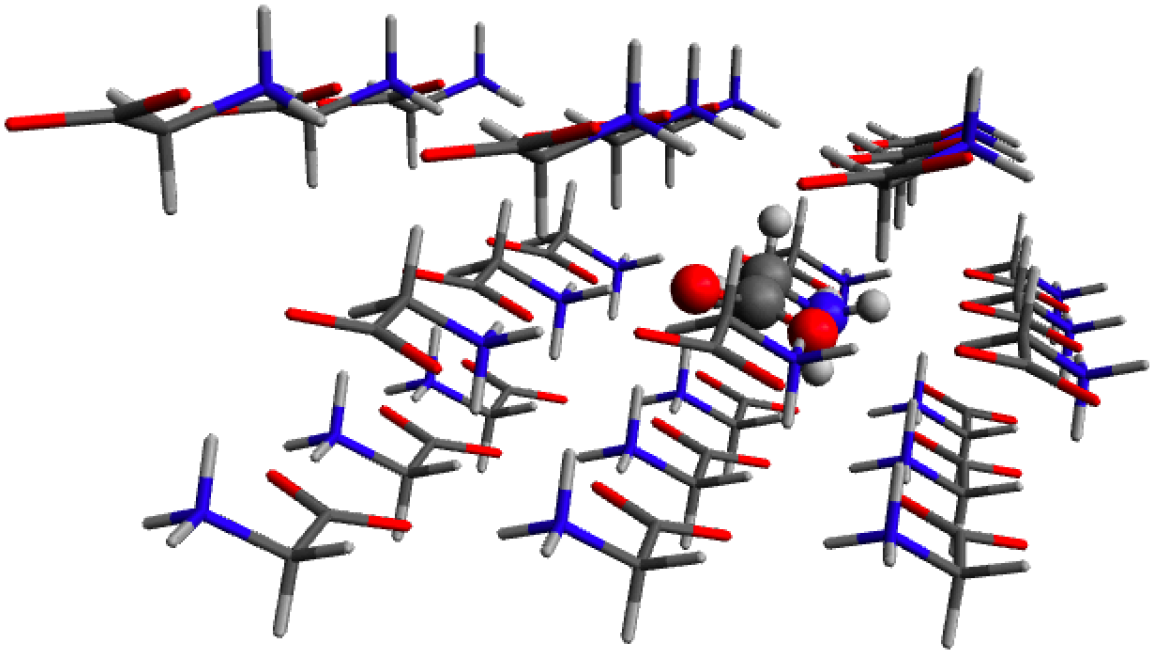

Figure S8. Three-dimensional structure of the cluster model used in the calculations of a glycine molecule (ball & stick representation) with an embedding composed of 26 other glycine molecules (stick representation) for providing the environment of the crystal structure of α-glycine. All atomic positions were taken from the crystallographic structure of α-glycine [27], and were kept frozen in the calculations with the exception of the hydrogen atoms in the central molecule.

9. References

1. Choi, M.; Kleitz, F.; Liu, D.; Lee, H. Y.; Ahn, W.-S.; Ryoo, R., Controlled Polymerization in Mesoporous Silica toward the Design of Organic-Inorganic Composite Nanoporous Materials. *J. Am. Chem. Soc.* **2005,** *127*, 1924-1932.
2. Young, P. D.; Notestein, J. M., The Role of Amine Surface Density in Carbon Dioxide Adsorption on Functionalized Mixed Oxide Surfaces. *Chem. Sus. Chem.* **2011,** *4*, 1671-1678.
3. Antao, S. M.; Hassan, I.; Wang, J.; Lee, P. L.; Toby, B. H., State-of-the-art high-resolution powder x-ray diffraction (HRPXRD) illustrated with Rietveld Structure Refinement of quartz, sodalite, tremolite, and meionite. *Can Mineral.* **2008,** *46*, 1501-1509.
4. Gomes, J. R. B.; Cordeiro, M. N. D. S.; Jorge, M., Gas-phase molecular structure and energetics of anionic silicates. *Geochim. Cosmochim. Acta* **2008,** *72*, 4421–4439.
5. Lopez, N.; Illas, F.; Pacchioni, G., Adsorption of Cu, Pd, and Cs Atoms on Regular and Defect Sites of the SiO2 Surface. *J. Am. Chem. Soc.* **1999,** *121*, 813-821.
6. Gomes, J. R. B.; Illas, F.; Silvi, B., Topological analysis of the metal-support interaction: the case of Pd atoms on oxide surfaces. *Chem. Phys. Lett.* **2004,** *388*, 132-138.
7. Mafra, L.; Čendak, T.; Schneider, S.; Wiper, P. V.; Pires, J.; Gomes, J. R. B.; Pinto, M. L., Structure of Chemisorbed CO2 Species in Amine-Functionalized Mesoporous Silicas Studied by Solid-State NMR and Computer Modeling. *J. Am. Chem. Soc.* **2017,** *139*, 389-408.
8. Zhao, Y.; Truhlar, D. G., Comparative DFT Study of van der Waals Complexes: Rare-Gas Dimers, Alkaline-Earth Dimers, Zinc Dimer, and Zinc-Rare-Gas Dimers. *J. Phys. Chem. A* **2006,** *110*, 5121-5129.
9. Zhao, Y.; Truhlar, D. G., The M06 suite of density functionals for main group thermochemistry, thermochemical kinetics, noncovalent interactions, excited states, and transition elements: two new functionals and systematic testing of four M06-class functionals and 12 other functionals. *Theor. Chem. Account* **2008,** *120*, 215-241.
10. Hariharan, P. C.; Pople, J. A., The Influence of Polarization Functions on Molecular Orbital Hydrogenation Energies. *Theor. Chim. Acta* **1973,** *28*, 213-222.
11. Francl, M. M.; Pietro, W. J.; Hehre, W. J.; Binkley, J. S.; Gordon, M. S.; DeFrees, D. J.; Pople, J. A., Self-consistent molecular orbital methods. XXIII. A polarization-type basis set for second-row elements. *J. Chem. Phys.* **1982,** *77*, 3654-3665.
12. Frisch, M. J.; Trucks, G. W.; Schlegel, H. B.; Scuseria, G. E.; Robb, M. A.; Cheeseman, J. R.; Scalmani, G.; Barone, V.; Mennucci, B.; Petersson, G. A.; Nakatsuji, H.; Caricato, M.; Li, X.; Hratchian, H. P.; Izmaylov, A. F.; Bloino, J.; Zheng, G.; Sonnenberg, J. L.; Hada, M.; Ehara, M.; Toyota, K.; Fukuda, R.; Hasegawa, J.; Ishida, M.; Nakajima, T.; Honda, Y.; Kitao, O.; Nakai, H.; Vreven, T.; J. A. Montgomery, J.; Peralta, J. E.; Ogliaro, F.; Bearpark, M.; Heyd, J. J.; Brothers, E.; Kudin, K. N.; Staroverov, V. N.; Kobayashi, R.; Normand, J.; Raghavachari, K.; Rendell, A.; Burant, J. C.; Iyengar, S. S.; Tomasi, J.; Cossi, M.; Rega, N.; Millam, J. M.; Klene, M.; Knox, J. E.; Cross, J. B.; Bakken, V.; Adamo, C.; Jaramillo, J.; Gomperts, R.; Stratmann, R. E.; Yazyev, O.; Austin, A. J.; Cammi, R.; Pomelli, C.; Ochterski, J. W.; Martin, R. L.; Morokuma, K.; Zakrzewski, V. G.; Voth, G. A.; Salvador, P.; Dannenberg, J. J.; Dapprich, S.; Daniels, A. D.; Farkas, Ö.; Foresman, J. B.; Ortiz, J. V.; Cioslowski, J.; Fox, D. J. *Gaussian 09, Revision B.01*, Gaussian, Inc.: Wallingford, CT, 2009.
13. Valero, R.; Gomes, J. R. B.; Truhlar, D. G.; Illas, F., Good performance of the M06 family of hybrid meta generalized gradient approximation density functionals on a difficult case: CO adsorption on MgO(001). *J. Chem. Phys.* **2008,** *129*, 124710.

14. Valero, R.; Gomes, J. R. B.; Truhlar, D. G.; Illas, F., Density functional study of CO and NO adsorption on Ni-doped MgO(100). *J. Chem. Phys.* **2010,** *132*, 104701.
15. Toda, J.; Fischer, M.; Jorge, M.; Gomes, J. R. B., Water adsorption on a copper formate paddlewheel model of CuBTC: A comparative MP2 and DFT study. *Chem. Phys. Lett.* **2013,** *587*, 7-13.
16. Pillai, R. S.; Jorge, M.; Gomes, J. R. B., Interaction of atmospheric gases with ETS-10: A DFT study. *Micropor. Mesopor. Mater.* **2014,** *190*, 38-45.
17. Perdew, J. P.; Schmidt, K., Jacob's Ladder of Density Functional Approximations for the Exchange-Correlation Energy. *AIP Conf. Proc.* **2001,** *577*, 1-20.
18. Willoughby, P. H.; Jansma, M. J.; Hoye, T. R., A guide to small-molecule structure assignment through computation of (1H and 13C) NMR chemical shifts. *Nature Protocols* **2014,** *9*, 643-660.
19. Mafra, L.; Čendak, T.; Schneider, S.; Wiper, P. V.; Pires, J. o.; Gomes, J. R. B.; Pinto, M. s. L., Amine functionalized porous silica for CO2/CH4 separation by adsorption: Which amine and why. *Chem. Eng. J.* **2018,** *336*, 612-621.
20. Kesharwani, M. K.; Brauer, B.; Martin, J. M. L., Frequency and Zero-Point Vibrational Energy Scale Factors for Double-Hybrid Density Functionals (and Other Selected Methods): Can Anharmonic Force Fields Be Avoided? *J. Phys. Chem. A* **2015,** *119*, 1701-1714.
21. Wolinski, K.; Hinton, J. F.; Pulay, P., Efficient Implementation of the Gauge-Independent Atomic Orbital Method for NMR Chemical Shift Calculations. *J. Am. Chem. Soc.* **1990,** *112*, 8251-8260.
22. Cheeseman, J. R.; Trucks, G. W.; Keith, T. A.; Frisch, M. J., A comparison of models for calculating nuclear magnetic resonance shielding tensors. *J. Chem. Phys.* **1996,** *104*, 5497-5509.
23. Lodewyk, M. W.; Siebert, M. R.; Tantillo, D. J., Computational Prediction of 1H and 13C Chemical Shifts: A Useful Tool for Natural Product, Mechanistic, and Synthetic Organic Chemistry. *Chem. Rev.* **2012,** *112*, 1839-1862.
24. Perinu, C.; Saramakoon, G.; Arstad, B.; Jens, K.-J., Application of 15N-NMR spectroscopy to analysis of amine based CO2 capture solvents. *Energy Procedia* **2014,** *63*, 1144-1150.
25. Tomasi, J.; Mennucci, B.; Cammi, R., Quantum mechanical continuum solvation models. *Chem. Rev.* **2005,** *105*, 2999-3093.
26. Čendak, T.; Sequeira, L.; Sardo, M.; Valente, A.; Pinto, M. s. L.; Mafra, L. s., Detecting proton-transfer in CO2 species chemisorbed on amine- modified mesoporous silicas using 13C NMR chemical shift anisotropy and smart control of amine surface density. *Chem. Eur. J.* **2018,** *24*, 10136-10145.
27. Langan, P.; Mason, S. A.; Myles, D.; Schoenborn, B. P., Structural characterization of crystals of [alpha]-glycine during anomalous electrical behaviour. *Acta Cryst.* **2002,** *B58*, 728-733.
28. Chen, C.-H.; Shimon, D.; Lee, J. J.; Didas, S. A.; Mehta, A. K.; Sievers, C.; Jones, C. W.; Hayes, S. E., Spectroscopic Characterization of Adsorbed 13CO2 on 3-Aminopropylsilyl-Modified SBA15 Mesoporous Silica. *Environ. Sci. Technol.* **2017,** *51*, 6553-6559.
29. Pinto, M. L.; Mafra, L. s.; Guil, J. M.; Pires, J.; Rocha, J., Adsorption and Activation of CO2 by Amine-Modified Nanoporous Materials Studied by Solid-State NMR and 13CO2 Adsorption. *Chem. Mater.* **2011,** *23*, 1387-1395.

30. Mello, M. l. R.; Phanon, D.; Silveira, G. Q.; Llewellyn, P. L.; Ronconi, C. l. M., Amine-modified MCM-41 mesoporous silica for carbon dioxide capture. *Micropor. Mesopor. Mater.* **2011,** *143*, 174-179.
31. Sayari, A.; Belmabkhout, Y.; Da'na, E., CO2 Deactivation of Supported Amines: Does the Nature of Amine Matter? *Langmuir* **2012,** *28*, 4241-4247.
32. Huang, S.-J.; Hung, C.-T.; Zheng, A.; Lin, J.-S.; Yang, C.-F.; Chang, Y.-C.; Deng, F.; Liu, S.-B., Capturing the Local Adsorption Structures of Carbon Dioxide in Polyamine-Impregnated Mesoporous Silica Adsorbents. *J. Phys. Chem. Lett.* **2014,** *5*, 3183-3187.
33. Santos, T. C. d.; Bourrelly, S.; Llewellyn, P. L.; Carneiro, J. W. d. M.; Ronconi, C. M., Adsorption of CO2 on amine-functionalised MCM-41: experimental and theoretical studies. *Phys. Chem. Chem. Phys.* **2015,** *17*, 11095-11102.
34. Moore, J. K.; Sakwa-Novak, M. A.; Chaikittisilp, W.; Mehta, A. K.; Conradi, M. S.; Jones, C. W.; Hayes, S. E., Characterization of a Mixture of CO2 Adsorption Products in Hyperbranched Aminosilica Adsorbents by 13C Solid-State NMR. *Environ. Sci. Technol.* **2015,** *49*, 13684-13691.
35. Milner, P. J.; Siegelman, R. L.; Forse, A. C.; Gonzalez, M. I.; Runcěvski, T.; Martell, J. D.; Reimer, J. A.; Long, J. R., A Diaminopropane-Appended Metal−Organic Framework Enabling Efficient CO2 Capture from Coal Flue Gas via a Mixed Adsorption Mechanism. *J. Am. Chem. Soc.* **2017,** *139*, 13541-13553.
36. Foo, G. S.; Lee, J. J.; Chen, C.-H.; Hayes, S. E.; Sievers, C.; Jones, C. W., Elucidation of Surface Species through in Situ FTIR Spectroscopy of Carbon Dioxide Adsorption on Amine-Grafted SBA-15. *Chem. Sus. Chem.* **2017,** *10*, 266-276.
37. Shimon, D.; Chen, C.-H.; Lee, J. J.; Didas, S. A.; Sievers, C.; Jones, C. W.; Hayes, S. E., 15N Solid State NMR Spectroscopic Study of Surface Amine Groups for Carbon Capture: 3-Aminopropylsilyl Grafted to SBA-15 Mesoporous Silica. *Environ. Sci. Technol.* **2018,** *52*, 1488-1495.
38. Hiyoshi, N.; Yogo, K.; Yashima, T., Adsorption characteristics of carbon dioxide on organically functionalized SBA-15. *Micropor. Mesopor. Mater.* **2005,** *84*, 357-365.
39. Knöfel, C.; Martin, C.; Hornebecq, V.; Llewellyn, P. L., Study of Carbon Dioxide Adsorption on Mesoporous Aminopropylsilane-Functionalized Silica and Titania Combining Microcalorimetry and in Situ Infrared Spectroscopy. *J. Phys. Chem. C* **2009,** *113*, 21726-21734.
40. Bacsik, Z.; Atluri, R.; Garcia-Bennett, A. E.; Hedin, N., Temperature-Induced Uptake of CO2 and Formation of Carbamates in Mesocaged Silica Modified with n-Propylamines. *Langmuir* **2010,** *26*, 10013-10024.
41. Bacsik, Z.; Ahlsten, N.; Ziadi, A.; Zhao, G.; Garcia-Bennett, A. E.; Martín-Matute, B. e.; Hedin, N., Mechanisms and Kinetics for Sorption of CO2 on Bicontinuous Mesoporous Silica Modified with n-Propylamine. *Langmuir* **2011,** *27*, 11118-11128.
42. Danon, A.; Stair, P. C.; Weitz, E., FTIR Study of CO2 Adsorption on Amine-Grafted SBA-15: Elucidation of Adsorbed Species. *J. Phys. Chem. C* **2011,** *115*, 11540-11549.
43. Aziz, B.; Hedin, N.; Bacsik, Z., Quantification of chemisorption and physisorption of carbon dioxide on porous silica modified by propylamines: Effect of amine density. *Micropor. Mesopor. Mater.* **2012,** *159*, 42-49.
44. Didas, S. A.; Sakwa-Novak, M. A.; Foo, G. S.; Sievers, C.; Jones, C. W., Effect of Amine Surface Coverage on the Co-Adsorption of CO2 and Water: Spectral Deconvolution of Adsorbed Species. *J. Phys. Chem. Lett.* **2014,** *5*, 4194-4200.

45. Tumuluri, U.; Isenberg, M.; Tan, C.-S.; Chuang, S. S. C., In Situ Infrared Study of the Effect of Amine Density on the Nature of Adsorbed CO2 on Amine-Functionalized Solid Sorbents. *Langmuir* **2014,** *30*, 7405-7413.
46. Hahn, M. W.; Jelic, J.; Berger, E.; Reuter, K.; Jentys, A.; Lercher, J. A., Role of Amine Functionality for CO2 Chemisorption on Silica. *J. Phys. Chem. B* **2016,** *120*, 1988-1995.
47. Mouline, Z.; Asai, K.; Daiko, Y.; Honda, S.; Bernard, S.; Iwamoto, Y., Amine-functionalized polycarbosilane hybrids for CO2-selective membranes. *J. Eur. Ceram. Soc.* **2017,** *37*, 5213-5221.
48. Potter, M. E.; Cho, K. M.; Lee, J. J.; Jones, C. W., Role of Alumina Basicity in CO2 Uptake in 3-Aminopropylsilyl-grafted Alumina Adsorbents. *Chem. Sus. Chem.* **2017,** *10*, 2192-2201.
49. Mitchell, M.; Muftakhidinov, B.; Winchen, T. Engauge Digitizer Software. http://markummitchell.github.io/engauge-digitizer (accessed April 26, 2018).
50. Leal, O.; Bolivar, C.; Ovalles, C.; Garcia, J. J.; Espidel, Y., Reversible adsorption of carbon dioxide on amine surface-bonded silica gel. *Inorg. Chim. Acta* **1995,** *240*, 183-189.
51. Huang, H. Y.; Yang, R. T.; Chinn, D.; Munson, C. L., Amine-Grafted MCM-48 and Silica Xerogel as Superior Sorbents for Acidic Gas Removal from Natural Gas. *Ind. Eng. Chem. Res.* **2003,** *42*, 2427-2433.
52. Lee, J. J.; Chen, C.-H.; Shimon, D.; Hayes, S. E.; Sievers, C.; Jones, C. W., Effect of Humidity on the CO2 Adsorption of Tertiary Amine Grafted SBA-15. *J. Phys. Chem. C* **2017,** *121*, 23480-23487.